



Research
Water Pollution Control—Article

An AuNPs/Mesoporous NiO/Nickel Foam Nanocomposite as a Miniaturized Electrode for Heavy Metal Detection in Groundwater



Boyuan Xue^{a,#}, Qian Yang^{a,#}, Kaidong Xia^{a,b,#}, Zhihong Li^b, George Y. Chen^c, Dayi Zhang^{d,*}, Xiaohong Zhou^{a,e,*}

^a State Key Joint Laboratory of Environment Simulation and Pollution Control, School of Environment, Tsinghua University, Beijing 100084, China

^b National Key Laboratory of Science and Technology on Micro/Nano Fabrication, Institute of Microelectronics, Peking University, Beijing 100871, China

^c Shenzhen Key Laboratory of Photonic Devices and Sensing Systems for Internet of Things, Guangdong and Hong Kong Joint Research Centre for Optical Fiber Sensors, Shenzhen University, Shenzhen 518060, China

^d College of New Energy and Environment, Jilin University, Changchun 130021, China

^e The Research Institute of Environmental Innovation (Suzhou), Tsinghua University, Suzhou 215000, China

ARTICLE INFO

Article history:

Received 27 January 2022

Revised 4 May 2022

Accepted 14 June 2022

Available online 5 July 2022

Keywords:

AuNPs

Mesoporous NiO

Miniaturized electrode

Heavy metal ions

Groundwater

Square wave voltammetry

ABSTRACT

Heavy metals, notably Pb^{2+} and Cu^{2+} , are some of the most persistent contaminants found in groundwater. Frequent monitoring of these metals, which relies on efficient, sensitive, cost-effective, and reliable methods, is a necessity. We present a nanocomposite-based miniaturized electrode for the concurrent measurement of Pb^{2+} and Cu^{2+} by exploiting the electroanalytical technique of square wave voltammetry. We also propose a facile *in situ* hydrothermal calcination method to directly grow binder-free mesoporous NiO on a three-dimensional nickel foam, which is then electrochemically seeded with gold nanoparticles (AuNPs). The meticulous design of a low-barrier Ohmic contact between mesoporous NiO and AuNPs facilitates target-mediated nanochannel-confined electron transfer within mesoporous NiO. As a result, the heavy metals Pb^{2+} (0.020 $\text{mg}\cdot\text{L}^{-1}$ detection limit; 2.0–16.0 $\text{mg}\cdot\text{L}^{-1}$ detection range) and Cu^{2+} (0.013 $\text{mg}\cdot\text{L}^{-1}$ detection limit; 0.4–12.8 $\text{mg}\cdot\text{L}^{-1}$ detection range) can be detected simultaneously with high precision. Furthermore, other heavy metal ions and common interfering ions found in groundwater showed negligible impacts on the electrode's performance, and the recovery rate of groundwater samples varied between $96.3\% \pm 2.1\%$ and $109.4\% \pm 0.6\%$. The compactness, flexible shape, low power consumption, and ability to remotely operate our electrode pave the way for onsite detection of heavy metals in groundwater, thereby demonstrating the potential to revolutionize the field of environmental monitoring.

© 2022 THE AUTHORS. Published by Elsevier LTD on behalf of Chinese Academy of Engineering and Higher Education Press Limited Company. This is an open access article under the CC BY-NC-ND license (<http://creativecommons.org/licenses/by-nc-nd/4.0/>).

1. Introduction

Heavy metal pollution, such as Pb^{2+} and Cu^{2+} , arises from large-scale mining activities, manufacturing industries, unregulated discharge of industrial wastes, misuse of underground water, and exhaustion of the groundwater level. Such pollution results in considerable damage to the groundwater environment [1]. High concentrations of heavy metal ions in groundwater pose a health hazard to millions of people worldwide, with particularly signifi-

cant impacts on vulnerable communities in developing regions where groundwater is used as the main source of drinking water. The diversity and complexity of groundwater matrices, mainly caused by human activities such as industrial production, agricultural planting, seawater intrusion, oil spills, and so forth, make it difficult to detect heavy metals in groundwater sources [2]. Various instrumental analytical techniques for heavy metals have been reported, including atomic adsorption spectrometry (AAS) [3,4], inductively coupled plasma-atomic emission spectrometry (ICP-AES) [5,6], and inductively coupled plasma-mass spectrometry (ICP-MS) [7,8]. However, such techniques are relatively complex, relying on sophisticated instruments and professional operators, which restricts their range of applications. Hence, the development of efficient, sensitive, cost-effective, and reliable detection methods

* Corresponding authors.

E-mail addresses: zhangdayi@tsinghua.org.cn (D. Zhang), xhzhou@mail.tsinghua.edu.cn (X. Zhou).

These authors contributed equally to this work.

with the potential for onsite monitoring of groundwater is in high demand, yet at the same time, poses a considerable challenge.

Recently, huge strides have been made in the adaptation of various optical and electrical sensor designs for the measurement of a range of heavy metals, including colorimetric [9], fluorescent [10], field-effect transistor-based [11], and electrochemical types [12]. Owing to their merits, including easy operation, fast response, low cost, and high sensitivity, sensors serve as a prominent alternative to the traditional instrument-based analytical techniques. Moreover, electrochemical sensors employing electroanalytical techniques possess inherent advantages, such as their robustness and resilience to sample turbidity [13]. Very recently, an increasing number of novel nanomaterials have emerged following the explosive advancement of materials science and synthetic characterization tools. Nanomaterial-based sensing devices for heavy metals exhibit the advantages of easy miniaturization and excellent detection performance, displaying the potential to revolutionize multiple fields of medical diagnostics, food safety, and environmental monitoring. Among them, two-dimensional (2D) nanosheet-layered materials with atomic-level thickness (generally < 5 nm), such as graphene, hexagonal boron nitride, metal (hydrogen) oxide, and transition metal dichalcogenides, are highly favored by researchers in the field of sensing owing to their attractive physical, chemical, optical, and electrical properties [14]. Among the multitude of different types of 2D nanosheets, 2D metal oxide nanosheets have attracted the most attention due to their excellent crystallinity, more suitable Debye length, high specific surface area, and electron steric-limited domain effect [15]. A 2D nickel-oxide (NiO) nanosheet is a p-type semiconductor that features an octahedral crystal structure and a bandgap of 3.6–4.2 eV [16]. The redox electron transfer between Ni²⁺ and Ni³⁺ on the octahedral structure gives NiO superior electrocatalytic properties compared with other metal oxides [17]. Its isoelectric point ranges from approximately 11 to 12, which is higher than that of other 2D sheet oxides (e.g., ZnO, ZrO₂, TiO₂) [18]. However, the practical use of this material is severely limited by its deficient carrier transport efficiency, thus resulting in low conductivity properties and low detection sensitivity [19].

Realizing a 2D NiO nanosheet with a uniform mesoporous structure is an effective way to obtain a higher specific surface area and more favorable electrical conductivity while further elevating the electrochemical and morphological advantages of 2D metal oxide nanosheets. As a result, the 2D mesoporous NiO nanosheet successfully serves as an electrode material in the field of energy storage, such as supercapacitors and Li-ion batteries, with a significantly increased specific surface area, electrochemical active sites, and bipolar plate effect [20,21]. However, using a 2D mesoporous NiO nanosheet as an electrochemical sensing material is impractical due to difficulties in material handling and deployment. For example, 2D mesoporous oxide nanosheets generally need to be mixed with auxiliary materials (e.g., binder) and then coated and dried on the electrode substrate after synthesis, which significantly affects the electrode conductivity [22]. Moreover, the use of surfactants or structure-directing agents usually results in the aggregation of nanosheets or the formation of flower-like microspheres, lowering the specific surface area and reducing the active sites of the electrode [23]. Alternatively, a binder-free *in situ* fabrication method that presynthesizes the precursor structures on the electrode substrate for the following derived 2D nanosheet structures has been proposed [24]. However, this method requires the addition of chemical reagents for precursor synthesis, which can lead to unstable contact with the electrode substrate. Although forming uniformly distributed mesoporous structures on 2D oxide nanosheets improves their physical and chemical properties, thus enhancing the electron transport properties to an extent, nonetheless the intrinsically poor electrical conductivity of the oxide

materials themselves drastically limits their applications for the construction of impedance-based or current-based electrochemical sensors [25].

To address these bottlenecks, nanostructured noble metals such as gold nanoparticles (AuNPs), which possess a work function greater than the combined total of the electron affinity energy of NiO and the bandgap energy, are able to provide lattices similar to those of electroactive NiO to generate epitaxial interfaces, thus forming a low-barrier Ohmic contact and small Schottky barrier [21]. Inspired by these phenomena, we demonstrate a miniaturized sensing electrode based on an AuNP-electrodeposited mesoporous NiO/nickel foam to simultaneously detect Pb²⁺ and Cu²⁺. In this platform, a facile *in situ* hydrothermal calcination method was used to directly grow binder-free mesoporous NiO on nickel foam with no addition of chemical reagents. Moreover, we creatively seeded the electrode with AuNPs using an electrodeposition reaction, overcoming the problem of the properties of low conductivity and low detection sensitivity of the NiO electrode via a low-resistive metal/semiconductor Ohmic contact. In addition to low cost and simple operation (no need for pretreatment), this electrode is optimized to measure Pb²⁺ and Cu²⁺ in diverse groundwater matrices with low detection limits of 0.020 mg·L⁻¹ for Pb²⁺ and 0.013 mg·L⁻¹ for Cu²⁺, respectively.

2. Materials and methods

2.1. Materials and reagents

Standard solutions of Pb²⁺, Cu²⁺, and other interfering ions (K⁺, Mg²⁺, Na⁺, Ca²⁺, SO₄²⁻, Cl⁻, CO₃²⁻, NO₃⁻, Cr⁶⁺, Ag⁺, Hg⁺, and Cd²⁺) were purchased from Aladdin Bio-Chem Technology Co., Ltd. (China). Hydrochloric acid (HCl, 36%), concentrated sulfuric acid (H₂SO₄, 98%), and gold chloride (HAuCl₄) were acquired from Sigma-Aldrich Co., Ltd. (China). Polyvinyl pyrrolidone (PVP)-K30 and electrolyte series (HAC, NaAC, K₃[Fe(CN)₆], and K₄[Fe(CN)₆]·3H₂O) were purchased from Sinopharm Chemical Reagent Beijing Co., Ltd. (China). Phosphate buffer solution (PBS, 0.1 mol·L⁻¹, pH 7) was prepared by mixing stock solutions of 0.1 mol·L⁻¹ Na₂HPO₄·12H₂O and 0.1 mol·L⁻¹ NaH₂PO₄·2H₂O [V(Na₂HPO₄·12H₂O):V(NaH₂PO₄·2H₂O) = 81:19]. All reagents were of analytical grade and prepared using ultrapure water (Milli-Q; Millipore, USA; 18.2 MΩ·cm⁻¹) without further purification.

Nickel foam (1.5 mm thickness, 110 pores per inch pore density and 380 g·m⁻² areal density) was purchased from Taiyuan Liyuan Lithium Battery Technology Center, China.

2.2. Instruments

X-ray diffraction (XRD) was carried out using a Rigaku D/Max-2400 X-ray diffractometer with the parameter settings of 40 kV tube voltage, 60 mA tube current, and 5°–110° scan angle range. The obtained elemental peak correlation data were compared to the diffractive matter standard comparison card (Joint Committee on Powder Diffraction Standards (JCPDS)).

X-ray photoelectron spectroscopy (XPS) was performed using a Thermo Scientific Escalab 250Xi analyzer (USA) with an X-ray spot wavelength parameter of 500 μm. All XPS spectra were calibrated by the C 1s line at 284.8 eV.

Field emission scanning electron microscopy (SEM) was carried out using a ZEISS GEMINISEM 550 (Germany) scanning electron microscope with the InLens imaging mode, an accelerating voltage of 15 kV, and a vacuum level of 1 × 10⁻⁷ Pa.

Energy dispersive X-ray spectrometry (EDS) was performed using a ZEISS GEMINISEM 550 X-ray energy spectrum analyzer (model INCA ENERGY; Oxford Instruments, UK).

Field emission transmission electron microscopy (TEM), high-resolution TEM (HRTEM), and selected area electron diffraction (SAED) were performed using an FEI Tecnai G2 F20 (USA) field-emission transmission electron microscope. The accelerating voltage was set to 200 kV and the filament voltage was set to 3.7 kV. High-resolution lattice size measurements were performed using Gatan digital micrograph software (version 2.3). To facilitate observation, a small portion of the AuNPs/mesoporous NiO/nickel foam nanocomposite was dispersed in an appropriate amount of anhydrous ethanol for sonication to remove the nanostructured AuNPs/mesoporous NiO composite or mesoporous NiO nanosheets from the nickel foam. Then, the ultrasonically-treated anhydrous ethanol solution was dropped on the silicon wafer and placed on the carbon film for testing.

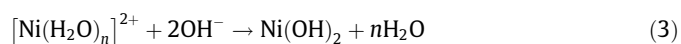
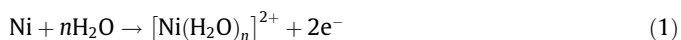
N₂ absorption–desorption isotherm data were collected using a MicrotracBEL BELSORP-Max instrument (Japan), and a Barrett–Joyner–Halenda (BJH) model was used to simulate the pore size distribution.

Inductively coupled plasma-optical emission spectrometry (ICP-OES) was performed using a Thermo Scientific SOE-129 spectrometer.

2.3. Preparation of the nanocomposite-based miniaturized electrode

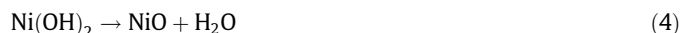
Considering the improved performance of a binder-free electrode in sensing and energy storage [22,26], we have demonstrated a facile *in situ* hydrothermal calcination method to form binder-free mesoporous NiO directly on nickel foam, followed by electrochemical deposition of AuNPs on the mesoporous NiO/nickel foam composite (Fig. 1). More specifically, the *in situ* hydrothermal calcination method included the direct growth of mesoporous nanosheets on nickel foam through the *in situ* oxidation of nickel foam to synthesize Ni(OH)₂ nanosheets in ultrapure water (without nickel and other additives) under hydrothermal conditions. Then, high-temperature calcination converted the Ni(OH)₂ flakes into mesoporous NiO nanosheets.

First, to directly grow β-Ni(OH)₂ nanosheets on nickel foam (Fig. 1, step I), a simple and convenient *in situ* hydrothermal reaction method, that is, *in situ* oxidation of nickel to produce Ni(OH)₂ nanosheets in ultrapure water (without nickel and other additives), was proposed, similar to our previous research [26]. Briefly, the nickel foam was cut into 3.5 cm × 1.5 cm pieces, thoroughly sonicated in 20% HCl for 10 min, and then let stand for 2 h to remove the surface oxide impurity layer. Then, the nickel foam was rinsed in anhydrous ethanol and ultrapure water with ultrasonication to remove the adsorbed HCl. Finally, the nickel foam was dried under constant temperature in an oven maintained at 70 °C for 2 h and then stored in a room temperature environment. Next, a portion of the nickel foam was submerged into the inner chamber of a Teflon stainless steel hydrothermal autoclave (50 mL) containing 75% ultrapure water, and the hydrothermal autoclave was sealed and held in a blast oven at a constant temperature of 110 °C for 24 h. After natural cooling to room temperature, the sample was extracted and subsequently dried at 70 °C. The reaction equations involved in the hydrothermal treatment method are listed below:

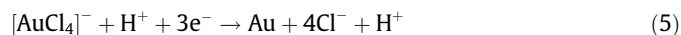


Next, to form mesoporous NiO nanosheets on nickel foam (Fig. 1, step II), the prepared β-Ni(OH)₂ nanosheets/nickel foam was cut into 1.5 cm × 1.5 cm pieces and placed in a crucible kettle. In a muffle furnace without any protective atmosphere or closure

of the crucible lid, the β-Ni(OH)₂ nanosheets/nickel foam was heated to 350 °C at 8 °C·min⁻¹ and maintained for 30 min and then naturally cooled to room temperature. The reaction equation during the high-temperature calcination process is listed below:



Last, to prepare the nanocomposite-based electrode (Fig. 1, step III), the fabricated mesoporous NiO/nickel foam electrode was subsequently cut into 0.5 cm × 1.5 cm pieces, removing the electrode clip contact area, and the remaining 0.5 cm × 1 cm size was used as the optimal area for the electrodeposition of AuNPs (Fig. S1 in Appendix A). The electrodeposition process was performed under a three-electrode system, that is, the AuNPs/mesoporous NiO/nickel foam electrode was used as the working electrode, a platinum sheet electrode was used as the counter electrode, and Ag/AgCl loaded with saturated KCl was used as the reference electrode. The electrolyte was 50 mL of HAuCl₄ (5 mmol·L⁻¹) aqueous solution, the electrodeposition potential was set to -0.2 V, the electrodeposition time was set to 120 s, and the electrodeposition temperature was 25 °C. Subsequently, the electrode was carefully cleaned with ultrapure water, dried with N₂, and stored at dry room temperature until use. The reaction is reflected by the following equation:



2.4. Sensing mechanism

Square wave voltammetry (SWV), an electroanalytical technique, was used for the measurement of Pb²⁺ and Cu²⁺, which could be divided into two main steps of predeposition and exfoliation (Fig. 1). During the predeposition process, the positive valence heavy metal ions (Pb²⁺ and Cu²⁺) in the electrolyte first diffused to the working cathode electrode surface to gain electrons, and hence, they were reduced to the zero-valence state under a constant potential. After predeposition, metals in the zero-valence state were reoxidized by a constant square wave voltage scan in the anode direction. A high dissolution current peak can be observed during the rapid oxidation process, and the peak potential of the stripping current is a function of the quantities of different types of heavy metal ions. The current signals at specific potentials, detected with the SWV method, were proportional to the concentrations of the target metal ions.

The electrochemical detection of Pb²⁺ and Cu²⁺ based on the SWV electrochemical analysis method was performed using the three-electrode system mentioned above. The parameters were as follows: a scanning potential interval of -0.8 to 0.6 V, amplitude of 25 mV, incremental potential of 8 mV, square wave application frequency of 25 Hz, and sensitivity of 10⁻². The electrolyte was a 0.1 mol·L⁻¹ HAC–NaAC buffer (pH 4.6), with a predeposition potential of -0.9 V and a deposition time of 300 s. At each stage, the dissociation potential for the exfoliation of heavy metals after the SWV test was 0.6 V, and the exfoliation time was 200 s. All tests were carried out at room temperature by using the electrochemical workstation of CHI600C with the control software version of CHI1140C (China). The error bars are the standard deviation of data from triplicate experiments.

3. Results and discussion

3.1. Characterization of the nanocomposite-based electrode

As revealed by the SEM images of the electrode before and after steps I and II in Fig. 1 (Figs. 2(a) and (b), inset shows the magnified image), the nickel foam was entirely overlaid with nanochaotic 2D

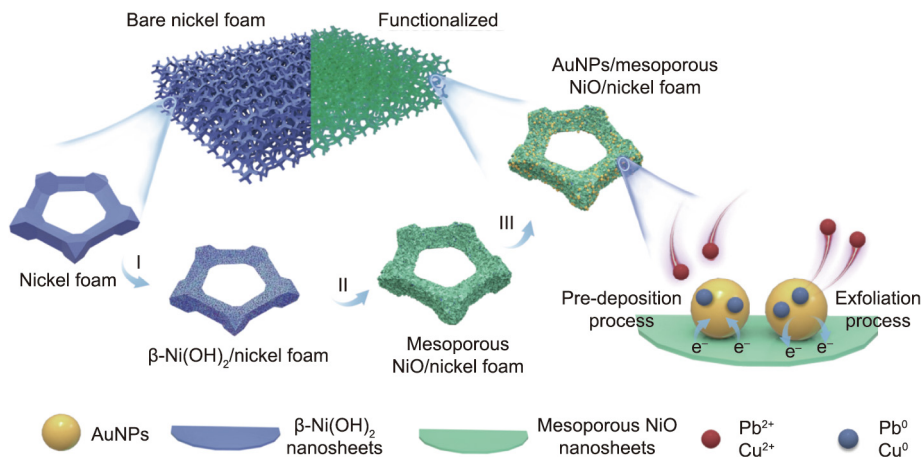


Fig. 1. Schematic illustration of the preparation of the nanocomposite-based electrode and the detection principles for heavy metal ions. Step I: binder-free β -Ni(OH)₂ nanosheets/nickel foam; step II: mesoporous NiO/nickel foam; and step III: AuNPs/mesoporous NiO/nickel foam nanocomposite-based electrode.

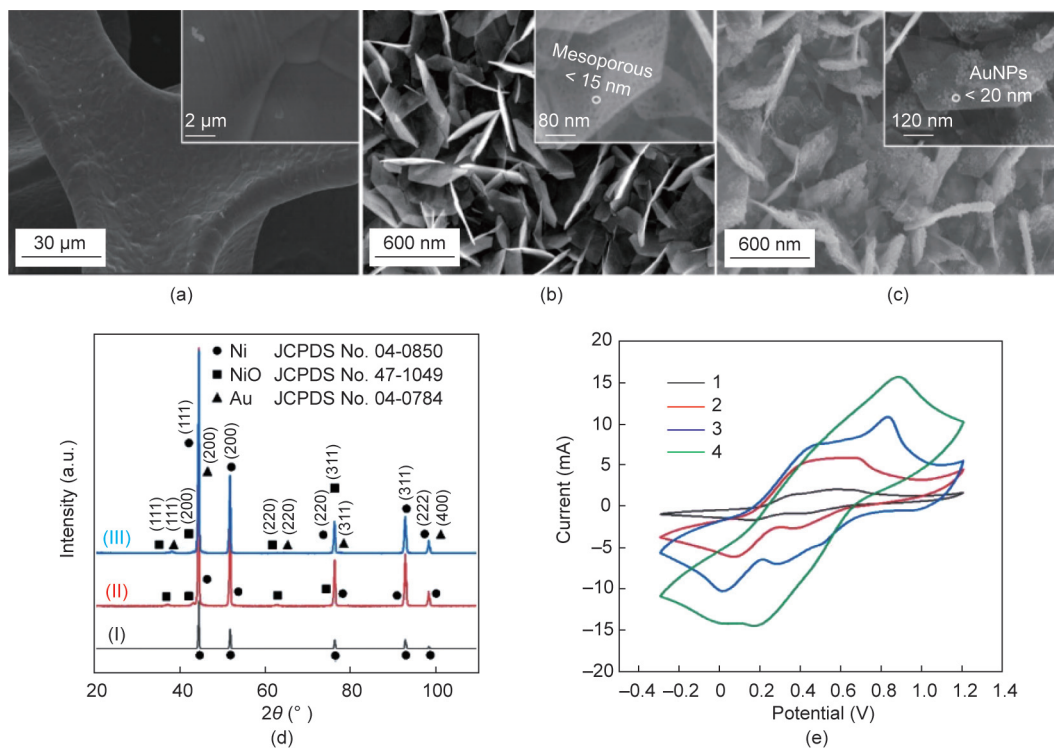


Fig. 2. Physical and chemical characterization of AuNPs/mesoporous NiO/nickel foam electrode at different preparation stages. SEM images of (a) nickel foam, (b) mesoporous NiO/nickel foam, and (c) AuNPs/mesoporous NiO/nickel foam; (d) XRD spectra of AuNPs/mesoporous NiO/nickel foam nanocomposite-based electrode (I: nickel foam; II: mesoporous NiO/nickel foam; III: AuNPs/mesoporous NiO/nickel foam); and (e) cyclic voltammetry (CV) curves of AuNPs/mesoporous NiO/nickel foam electrode at different fabrication stages (1: nickel foam; 2: β -Ni(OH)₂ nanosheets/nickel foam; 3: mesoporous NiO/nickel foam; 4: AuNPs/mesoporous NiO/nickel foam).

NiO flakes with a uniform mesoporous distribution after facile nickel salt- and additive-free hydrothermal treatment. The uniformly distributed mesoporous structures on the NiO nanosheets were smaller than 15 nm in size (inset of Fig. 2(b)). Notably, the hydrothermal growth time is a critical issue that has an impact on the morphology of the electrode, which was thoroughly studied and optimized (Fig. S2 in Appendix A). Fig. 2(c) clearly demonstrates the successful electrochemical deposition of uniformly dispersed AuNPs on the surface of the mesoporous NiO nanosheets after step III in Fig. 1, which did not destroy the original network structure of the nanosheet forest on the mesoporous NiO/nickel foam electrode. It is worth mentioning that an ultrasonic treatment (< 5 s) was applied before SEM analysis, which might have led to

the somewhat uniform distribution of AuNPs on the surface. However, the hexagonal close-packed (HCP) NiO nanosheet crystal structure, mesoporous structure, and AuNP crystal structure were not affected, showing the excellent stability of the nanostructure morphology of the electrode. The surfaces of nickel foam, mesoporous NiO/nickel foam, and AuNPs/mesoporous NiO/nickel foam were analyzed by XRD (Fig. 2(d)). As confirmed by the XRD spectra, the peaks occurred at $2\theta = 38.20^\circ, 44.40^\circ, 64.60^\circ, 77.50^\circ,$ and 98.10° (indicated with a triangle), consistent with the (111), (200), (220), (311), and (400) planes of Au (JCPDS No. 04-0784) [27].

The electrochemical behavior of the nanocomposite-based electrode was revealed by cyclic voltammetry (CV), as shown in Fig. 2(e). The CV process was performed using the three-electrode

system mentioned above, the scan rate was set to $49 \text{ mV}\cdot\text{s}^{-1}$, and the electrolyte was $0.1 \text{ mol}\cdot\text{L}^{-1}$ neutral PBS buffer solution containing $5 \text{ mmol}\cdot\text{L}^{-1} \text{ K}_3[\text{Fe}(\text{CN})_6]/\text{K}_4[\text{Fe}(\text{CN})_6]$. Compared to that of nickel foam before the hydrothermal reaction (Fig. 2(e), curve 1), the redox current increased after the formation of $\beta\text{-Ni}(\text{OH})_2$ nanosheets/nickel foam (Fig. 2(e), curve 2), demonstrating that abundant 2D $\beta\text{-Ni}(\text{OH})_2$ nanosheets supported the transformation of the $\text{Ni}(\text{OH})_2/\text{NiO}(\text{OH})$ pair, which produced a superior redox current related to the enhanced electron transfer property. However, the improvement factor was restricted owing to the low conductivity of the 2D $\beta\text{-Ni}(\text{OH})_2$ nanosheets. When the $\beta\text{-Ni}(\text{OH})_2$ nanosheet/nickel foam electrode was calcined at high temperatures to form mesoporous NiO/nickel foam, the redox current signal was significantly higher (Fig. 2(e), curve 3), which was likely caused by ① an enlargement of the specific surface area of the electrode induced by the formation of mesoporous structures and ② a large number of oxygen-deficient vacancies, which was equivalent to a high concentration of hole doping of NiO [28]. After the electrodeposition of AuNPs on mesoporous NiO/nickel foam, the redox peak current incrementally increased (Fig. 2(e), curve 4). This phenomenon was explained by ① the further increase in the specific surface area and ② the low-barrier Ohmic contact between the mesoporous NiO nanosheets and AuNPs [29]. The CV of the electrode at different scan rates (Fig. S3 in Appendix A) and their effective surface areas, as confirmed by the Sevcik equation (Note S1 and Fig. S4 in Appendix A), also showed the electrochemical and physical change of the electrode at different fabrication steps.

The properties of AuNPs/mesoporous NiO/nickel foam were further studied by TEM, HRTEM, and SAED, applied to the same regions of interest. As revealed by TEM (Fig. 3(a)), AuNPs were randomly distributed on the surface of the mesoporous NiO nanosheets, facilitating close interactions. The homodispersion of the AuNPs on the mesoporous NiO nanosheets was attributed to the following: ① The electrolyte was mixed with a medium chain length of PVP-K30 to improve the formation rate of nanoparticles, which helped avoid aggregation to form a gold film; ② the reunion of AuNPs was physically blocked by 2D disordered mesoporous NiO nanosheets; and ③ a Pt sheet electrode served as the counter electrode at the attachment of AuNPs, helping the electrodeposition due to the radii and lattice discrepancy of Au (4.08 \AA) and Pt (3.92 \AA) (the radii and lattice discrepancy between Au and Pt can be as great as 4.08%) [30]. As further confirmed by the HRTEM image of our electrode (Fig. 3(b)), lattice stripes of 0.24 and 0.204 nm were clearly visible in the dusk area, which was in excellent agreement with the (111) and (200) crystallographic surface indices of Au (JCPDS No. 04-0784). Meanwhile, the lattice stripes of 0.24 and 0.21 nm in the bright area were consistent with the (111) and (200) crystallographic surface indices of bunsenite (JCPDS No. 47-1049) [31]. In addition, two diffraction rings with obvious bright spots suggested the good crystallinity of the corresponding nanostructures and corresponded to the crystallographic surface indices of Au (220) and bunsenite (200) (inset of Fig. 3(b)), which was consistent with the XRD patterns in Fig. 2(d).

To further investigate the surface structure of the AuNPs/mesoporous NiO/nickel foam electrode at different preparation steps, N_2 adsorption–desorption tests were performed (Fig. S5 in Appendix A). The Barrett–Joyner–Halenda (BJH) method was used to analyze the isotherms to report pore size distributions. The isotherm conformations of both mesoporous NiO/nickel foam and AuNPs/mesoporous NiO/nickel foam electrodes showed that they were type IV isotherms (Brunauer classification) with H3 hysteresis loops (International Union of Pure and Applied Chemistry (IUPAC) classification) provided in the form of insets in Fig. S5, illustrating that the electrode materials had a high specific surface area and

mesoporous structure. The pore size distribution of mesoporous NiO/nickel foam was $2\text{--}130 \text{ nm}$ (centered at $2\text{--}10 \text{ nm}$) (Fig. S5(a)). After the electrodeposition process, the pore size of AuNPs/mesoporous NiO/nickel foam changed to $2\text{--}150 \text{ nm}$ (centered at $10\text{--}50 \text{ nm}$) (Fig. S5(b)). This phenomenon was caused by the deposition of AuNPs, which covered part of the mesopores and formed a three-dimensional (3D) structure network, eventually expanding the range of pore size distribution.

As further exhibited by EDS, in addition to the significant quantity of Ni (NiO and nickel foam) on the surface of the electrode, obvious characteristic peaks of Au (AuNPs) were also detected (Fig. 3(c)). The full XPS spectrum in Fig. 3(d) shows the peaks of C, Ni, Au, and O at distinct binding energies. The C 1s peak was explained by carbon pollution during the usage and storage of the sample [32]. Ni peaks (Fig. 3(e)) uncovered two characteristic binding energies of 856.5 and 873.8 eV with a 17.3 eV binding-energy gap, corresponding to Ni $2p_{3/2}$ and Ni $2p_{1/2}$ peaks [24]. The main peaks were along with two broad peaks of 861.4 and 880.5 eV , corresponding to Ni $2p_{3/2}$ and Ni $2p_{1/2}$ satellite peaks. These phenomena were consistent with the presence of HCP-structured NiO nanosheets on the substrate of the electrode. In addition, there were two characteristic peaks (Fig. 3(f)) at binding energies of 84.94 and 88.58 eV with a 3.64 eV binding-energy gap, corresponding to Au^0 peaks [33]. The characteristic spectrum of O 1s, as shown in Fig. 3(g), revealed distinct peaks at 530.1 and 531.8 eV . The peak at 531.8 eV indicated the Ni–O bond present in NiO, while the peak at 530.1 eV indicated the absorbed oxygen loosely bound to the electrode surface, caused by the high specific surface area structure of the electrode [25].

3.2. Electrochemical detection of heavy metal ions

The Pb^{2+} and Cu^{2+} sensing abilities of the AuNPs/mesoporous NiO/nickel foam electrode were characterized by testing the SWV response current signals of the electrode toward different concentrations of Pb^{2+} and Cu^{2+} in the electrolyte. As shown in Fig. 4(a), with increasing concentrations of both Pb^{2+} and Cu^{2+} , the corresponding SWV current signals increased. Peak current signals in the potential range of -0.5 to -0.4 V were generated by Pb^{2+} , while peak current signals in the potential range of 0.1 to 0.3 V were generated by Cu^{2+} [34,35]. After fitting the peak current signals with the concentrations, the quantitative range of the electrode was approximately $2.0\text{--}16.0 \text{ mg}\cdot\text{L}^{-1}$ for Pb^{2+} (Fig. 4(b)) and $0.4\text{--}12.8 \text{ mg}\cdot\text{L}^{-1}$ for Cu^{2+} (Fig. 4(c)). The limits of detection (LODs) for Pb^{2+} and Cu^{2+} were calculated as 0.020 and $0.013 \text{ mg}\cdot\text{L}^{-1}$, respectively, obeying the requirement that the signal-to-noise ratio (S/N) = 3. The increased electric conductivity performance (Fig. 2(e), curve 4) was followed by an ultrasensitivity toward the target, attributed to the low-barrier Ohmic contact between mesoporous NiO and AuNPs (Fig. 5) and nanochannel-confined electron transfer in the electrode design.

To elaborate, when the energy band levels of the semiconductor and metal have considerable Fermi energy discrepancies, an ineffective conductive rectifying contact occurs despite studies showing that the composite resistance can be regulated by the cooperative effect of the semiconductor and metal [36]. The poor conductive rectifying contact can only be compensated for when the combined total Fermi energy level and conduction band energy of the semiconductor are equal to or less than the work function of the metal because of their bandgap alignment [37]. For p-type semiconductors, their work function must be smaller than that of metals ($\Phi_s < \Phi_m$) to form a low-barrier Ohmic contact [38,39]. As illustrated in Fig. 5, AuNPs with a high work function of about 5.10 eV [40] can yield a low-barrier Ohmic contact with the p-type NiO semiconductor. This can lead to a work function of less than 4.92 eV , providing that the Fermi energy level and the

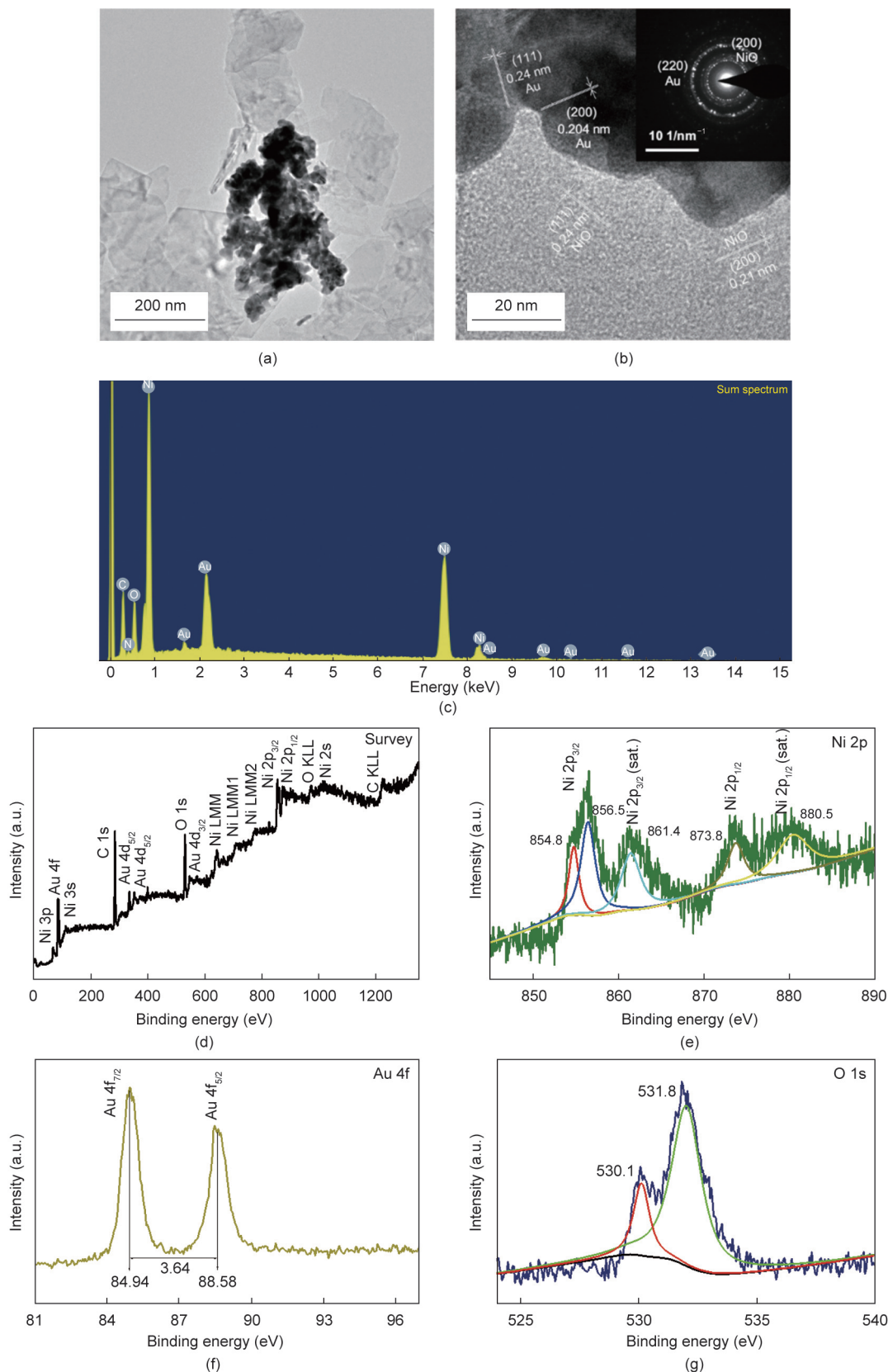


Fig. 3. Surface characterization of AuNPs/mesoporous NiO/nickel foam electrode: (a) TEM, (b) HRTEM, and inset of (b) SAED images of the AuNPs/mesoporous NiO/nickel foam electrode; (c) EDS spectrum of the HRTEM region; XPS spectra of the AuNPs/mesoporous NiO/nickel foam electrode: (d) full spectrum, (e) Ni 2p, (f) Au 4f, and (g) O 1s. sat.: satellite.

conduction band energy of NiO are 1.40 eV and less than 3.52 eV, respectively [41]. NiO was deduced as the most suitable metal

oxide for establishing an Ohmic contact with AuNPs (Table S1 in Appendix A), which gave rise to a fast electron transfer path in

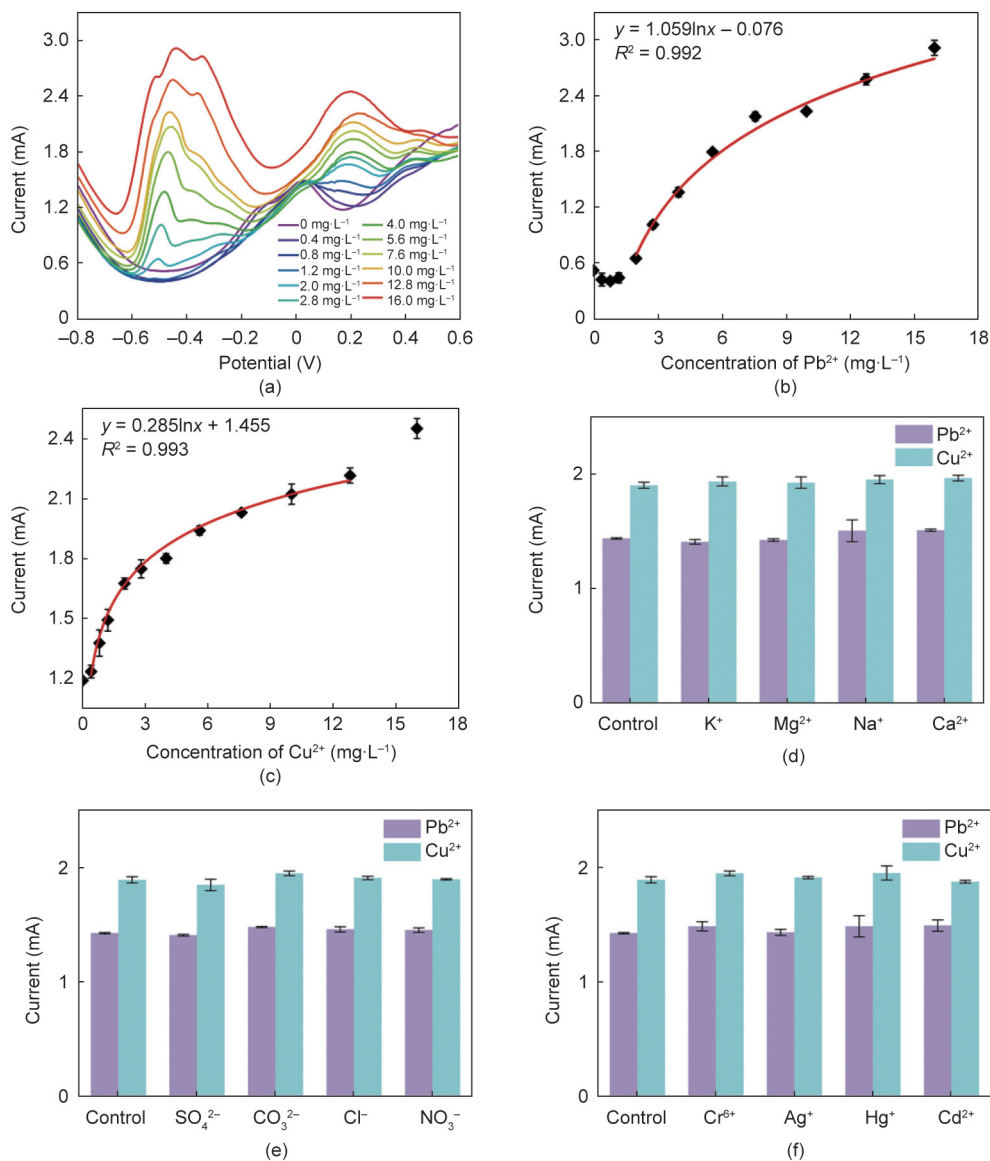


Fig. 4. Performance of AuNPs/mesoporous NiO/nickel foam electrode for Cu^{2+} and Pb^{2+} detection. (a) Comparison of SWV response current signals of the electrode toward different concentrations of Pb^{2+} and Cu^{2+} in electrolyte; calibration curves of the electrode for the detection of (b) Pb^{2+} and (c) Cu^{2+} in the range of 0–16 $\text{mg}\cdot\text{L}^{-1}$ ($n = 3$); selectivity of Pb^{2+} and Cu^{2+} detection (4 $\text{mg}\cdot\text{L}^{-1}$) employing this method against other interfering ions ($n = 3$): (d) cations (40 $\text{mg}\cdot\text{L}^{-1}$), (e) anions (40 $\text{mg}\cdot\text{L}^{-1}$), and (f) other heavy metal ions (4 $\text{mg}\cdot\text{L}^{-1}$).

addition to superior electric conduction performance in the AuNPs/NiO nanocomposite structure [37]. A 3D nanoscale electrode with high conductivity was implemented using a low-barrier Ohmic contact between NiO and AuNPs, performing as a bridge between partly disjointed NiO nanosheet structures, even though 2D NiO nanosheets were not entirely paved with AuNPs, as revealed by TEM and HRTEM (Figs. 3(a) and (b)) [29].

During the concurrent detection of Pb^{2+} and Cu^{2+} using the AuNPs/mesoporous NiO/nickel foam electrode, various interfering ions (including K^+ , Mg^{2+} , Na^+ , Ca^{2+} , SO_4^{2-} , CO_3^{2-} , Cl^- , NO_3^- , Cr^{6+} , Ag^+ , Hg^+ , and Cd^{2+}) were added to evaluate the electrode selectivity (Figs. 4(d)–(f)). K^+ , Mg^{2+} , Na^+ , and Ca^{2+} are common cations in groundwater; SO_4^{2-} , CO_3^{2-} , Cl^- , and NO_3^- are common anions in groundwater; and Cr^{6+} , Ag^+ , Hg^+ , and Cd^{2+} are common heavy metal species in groundwater [42,43]. With additional interfering ions, the current-based response of the electrode to Pb^{2+} and Cu^{2+} remained almost unchanged ($\pm 5\%$ relative standard deviations with the control group), and no dissolution current peaks corresponding to the interfering ions were found at other SWV scanning

potentials. We attributed such good selectivity to the high specific surface area and a large number of independent reaction spaces from the mesoporous structure of NiO nanosheets. Consequently, Pb^{2+} and Cu^{2+} easily contacted the electrode surface for constant potential reduction, effectively avoiding complexation with other heavy metal ions present in complex groundwater environments. This good stability and selectivity might also be associated with the high stability of the electrode structure. The precursor structure of NiO prepared by the *in situ* hydrothermal method was firmly deposited on nickel foam, and the mesoporous NiO nanosheets prepared by high-temperature calcination formed a stable core-shell-like structure by depositing AuNPs, which effectively enhanced the morphological stability of the electrode surface. Notably, previous researches revealed that the positions of peak current signals caused by the detected ions were greatly affected by the material of working electrode [44,45]. We attributed such good selectivity towards Pb^{2+} and Cu^{2+} to the unique characteristics of the AuNPs/mesoporous NiO/nickel foam nanocomposite fabricated in this work.

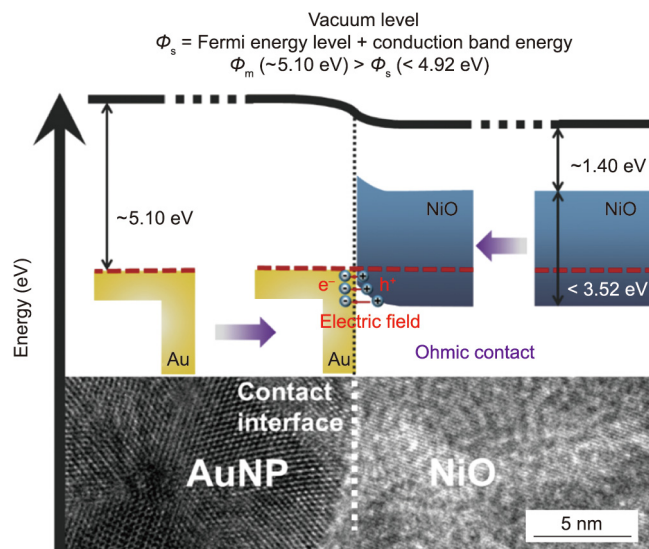


Fig. 5. Schematic diagram of the Ohmic contact between AuNPs and the NiO nanosheet semiconductor after energy band matching. In the case of a p-type semiconductor, the work function is the sum of the Fermi energy level and the conduction band energy. Notably, a TEM image illustrating the structural contact between AuNPs and the NiO nanosheet semiconductor is inserted in the lower part of the figure.

To evaluate the ability of the AuNPs/mesoporous NiO/nickel foam electrode to detect Pb^{2+} and Cu^{2+} in real groundwater samples, we collected groundwater samples 1 and 2 from Chifeng, Inner Mongolia, and sample 3 from Beijing. The site of samples 1 and 2 is a hazardous waste treatment plant with high-Pb dust ($120^\circ 02' 42.8'' \text{E}$, $41^\circ 48' 54.6'' \text{N}$), with an annual treatment capability of approximately 30 000 tonnes. The aquifer consists of fine sand and gravel layers, and the groundwater level is 11.0 to 18.0 m below ground, fluctuating between seasons. During the daily operating process, high-Pb dust at the dumping site was reported to contaminate the surface soils and then be transported into groundwater through rainfall and infiltration. The site of sample 3 is the campus of Tsinghua University ($116^\circ 20' 4.8'' \text{E}$, $39^\circ 59' 53.1'' \text{N}$). The aquifer consists of sand and gravel layers, and the groundwater supplies the tap water of Tsinghua University after processing steps. Accordingly, to meet the need for heavy metal measurements in the groundwater of these two sites, it is necessary to design surveillance devices for real-time online analysis and emergency response. Before measurement, $0.1 \mu\text{m}$ nylon injection filters were used to remove potential microorganisms and large suspended particles from water samples, followed by pretreatment

with a cation exchange resin (Dionex On Guard, II-H; Thermo Fisher Scientific, USA). Subsequently, the water pH was adjusted to 4.6 with HAC–NaAC buffer, and the samples were spiked with Pb^{2+} and Cu^{2+} at two different standard concentrations (2 and $4 \text{ mg}\cdot\text{L}^{-1}$) for analysis using the SWV method (Table 1). A good recovery ranged from 98.7% to 109.4% for Pb^{2+} and from 96.3% to 106.0% for Cu^{2+} . The coefficient variations for all recoveries were below 3.0%, indicating the good stabilities of this electrode in groundwater matrices. Moreover, the results were in excellent agreement with those determined by ICP-OES, demonstrating the practical potential and application prospect of this technology for detecting Pb^{2+} and Cu^{2+} simultaneously in groundwater environments. The superior electrochemical properties of our electrode, generated by the mesoporous structure and metal/semiconductor Ohmic contact, make it possible for accurate and rapid detection. Considering the miniaturized electrode, this technology has the potential to be used in the in-field or online quantification of Pb^{2+} and Cu^{2+} in groundwater in conjunction with a portable impedance device.

The AuNPs/mesoporous NiO/nickel foam electrode had an excellent detection range, sensitivity, repeatability, and stability, showing a comparable sensing performance compared to other reported electrodes for Pb^{2+} and Cu^{2+} detection (Table S2 in Appendix A). Because of the *in situ* hydrothermal calcination method used to directly grow mesoporous NiO and the electrodeposition method used to embed the NiO with AuNPs, our electrode has the advantages of low cost and convenient preparation over other electrodes. In addition, the most satisfying merit of the AuNPs/mesoporous NiO/nickel foam electrode is its ability to detect different heavy metal ions simultaneously.

Similar to other 2D nanosheets, 2D NiO has excellent chemical and structural stability, as well as a high specific surface area, a high isoelectric point, and the potential for surface modification capability. Therefore, mesoporous NiO nanosheets can be used as a good platform to link and fix biomolecules with low isoelectric points (such as nucleic acids), which have excellent adsorption stability [46]. In addition, our study has solved the problem of poor electrical conductivity of NiO nanosheets by forming a low-barrier Ohmic contact between mesoporous NiO and AuNPs. Accordingly, AuNPs/mesoporous NiO/nickel foam electrodes not only play important roles beyond the field of electrochemical sensing but also show great potential in biosensing.

4. Conclusions

We have presented a new electrochemical sensing platform based on the nanochannel electron transfer effect on a AuNPs/mesoporous NiO/nickel foam electrode to detect heavy metals in

Table 1
 Determination of Pb^{2+} and Cu^{2+} in three groundwater samples ($n = 3$).

Sample	Spiked ($\text{mg}\cdot\text{L}^{-1}$)	Found (ICP-OES) ($\text{mg}\cdot\text{L}^{-1}$)		Found (this work) ($\text{mg}\cdot\text{L}^{-1}$)		Recovery (this work) (%)		Coefficient variation (this work) (%)	
		Pb^{2+}	Cu^{2+}	Pb^{2+}	Cu^{2+}	Pb^{2+}	Cu^{2+}	Pb^{2+}	Cu^{2+}
1	0	< LOD	< LOD	< LOD	< LOD	—	—	—	—
	2.0	1.89	1.99	2.066 ± 0.028	1.995 ± 0.017	103.3	99.8	1.4	0.9
	4.0	3.96	3.85	4.039 ± 0.082	3.865 ± 0.056	101.0	96.6	2.0	1.4
2	0	< LOD	< LOD	< LOD	< LOD	—	—	—	—
	2.0	1.99	2.09	2.147 ± 0.012	2.120 ± 0.038	109.4	106.0	0.5	1.9
	4.0	3.94	3.90	4.059 ± 0.101	3.852 ± 0.084	101.5	96.3	2.4	2.1
3	0	< LOD	< LOD	< LOD	< LOD	—	—	—	—
	2.0	2.09	1.98	2.172 ± 0.015	1.972 ± 0.022	108.6	98.6	0.7	1.1
	4.0	3.87	3.83	3.947 ± 0.073	3.853 ± 0.086	98.7	96.3	1.8	2.1

groundwater. The preparation process was potentially economical and readily manufacturable on a large scale. In addition to the high specific surface area of the mesoporous nanocomposite, the *in situ* formation of 2D NiO nanosheets on nickel foam and the low-barrier Ohmic contact between NiO nanosheets and AuNPs resulted in a supersensitive measurement. To test the application potential of the electrode as a general type of electrochemical electrode platform, our electrode was used for the detection of Pb^{2+} (0.020 $\text{mg}\cdot\text{L}^{-1}$ detection limit; 2.0–16.0 $\text{mg}\cdot\text{L}^{-1}$ detection range) and Cu^{2+} (0.013 $\text{mg}\cdot\text{L}^{-1}$ detection limit; 0.4–12.8 $\text{mg}\cdot\text{L}^{-1}$ detection range) with satisfactory selectivity and high sensitivity in complicated and variable sample matrices. Furthermore, owing to the characteristics of miniaturization, low energy consumption, and good performance, electrodes can be widely used in the field of natural water real-time online analysis, wastewater treatment process detection, onsite rapid monitoring, emergency water pollution warning and so forth.

Acknowledgment

This research was supported by the National Key Research and Development Project of China (2019YFC1804802).

Compliance with ethical guidelines

Boyuan Xue, Qian Yang, Kaidong Xia, Zhihong Li, George Y. Chen, Dayi Zhang, and Xiaohong Zhou declare that they have no conflicts of interest or financial conflicts to disclose.

Appendix A. Supplementary data

Supplementary data to this article can be found online at <https://doi.org/10.1016/j.eng.2022.06.005>.

References

- [1] Herdan J, Feeney R, Kounaves SP, Flannery AF, Storment CW, Kovacs GTA, et al. Field evaluation of an electrochemical probe for *in situ* screening of heavy metals in groundwater. *Environ Sci Technol* 1998;32(1):131–6.
- [2] Wang Z, Su Q, Wang S, Gao Z, Liu J. Spatial distribution and health risk assessment of dissolved heavy metals in groundwater of eastern China coastal zone. *Environ Pollut* 2021;290:118016.
- [3] Pyle SM, Nocerino JM, Deming SN, Palasota JA, Palasota JM, Miller EL, et al. Comparison of AAS, ICP-AES, PSA, and XRF in determining lead and cadmium in soil. *Environ Sci Technol* 1996;30(1):204–13.
- [4] Radu T, Diamond D. Comparison of soil pollution concentrations determined using AAS and portable XRF techniques. *J Hazard Mater* 2009;171(1–3):1168–71.
- [5] Li S, Hu B, Jiang Z, Liang P, Li X, Xia L. Selective separation of La^{3+} and lanthanum organic complexes with nanometer-sized titanium dioxide and their detection by using fluorination-assisted electrothermal vaporization ICP-AES with *in-situ* matrix removal. *Environ Sci Technol* 2004;38(7):2248–51.
- [6] Cindrić IJ, Zeiner M, Kröppl M, Stingeder G. Comparison of sample preparation methods for the ICP-AES determination of minor and major elements in clarified apple juices. *Microchem J* 2011;99(2):364–9.
- [7] Lenz M, Floor GH, Winkel LHE, Román-Ross G, Corvini PFX. Online preconcentration-ICP-MS for selenium quantification and speciation at ultratrace. *Environ Sci Technol* 2012;46(21):11988–94.
- [8] Dai B, Cao M, Fang G, Liu B, Dong X, Pan M, et al. Schiff base-chitosan grafted multiwalled carbon nanotubes as a novel solid-phase extraction adsorbent for determination of heavy metal by ICP-MS. *J Hazard Mater* 2012;219–220:103–10.
- [9] Idros N, Chu D. Triple-indicator-based multidimensional colorimetric sensing platform for heavy metal ion detections. *ACS Sens* 2018;3(9):1756–64.
- [10] Wu W, Chen A, Tong L, Qing Z, Langone KP, Bernier WE, et al. Facile synthesis of fluorescent conjugated polyelectrolytes using polydentate sulfonate as highly selective and sensitive copper(II) sensors. *ACS Sens* 2017;2(9):1337–44.
- [11] Patil PD, Ghosh S, Wasala M, Lei S, Vajtai R, Ajayan PM, et al. Gate-induced metal-insulator transition in 2D van der Waals layers of copper indium selenide based field-effect transistors. *ACS Nano* 2019;13(11):13413–20.
- [12] Ding R, Cheong YH, Ahamed A, Lisak G. Heavy metals detection with paper-based electrochemical sensors. *Anal Chem* 2021;93(4):1880–8.
- [13] Hambly B, Guzinski M, Perez F, Pendley B, Lindner E. Deposition of EDOT-decorated hollow nanocapsules into PEDOT films for optical and electrochemical sensing. *ACS Appl Nano Mater* 2020;3(7):6328–35.
- [14] Shen J, Zhu Y, Jiang H, Li C. 2D nanosheets-based novel architectures: synthesis, assembly and applications. *Nano Today* 2016;11(4):483–520.
- [15] Peng L, Xiong P, Ma L, Yuan Y, Zhu Y, Chen D, et al. Holey two-dimensional transition metal oxide nanosheets for efficient energy storage. *Nat Commun* 2017;8(1):15139.
- [16] Tyagi M, Tomar M, Gupta V. Influence of hole mobility on the response characteristics of p-type nickel oxide thin film based glucose biosensor. *Anal Chim Acta* 2012;726:93–101.
- [17] Li S, Xia N, Lv X, Zhao M, Yuan B, Pang H. A facile one-step electrochemical synthesis of graphene/NiO nanocomposites as efficient electrocatalyst for glucose and methanol. *Sens Actuators B Chem* 2014;190:809–17.
- [18] Chen Z, Cao G, Gan L, Dai H, Xu N, Zang M, et al. Highly dispersed platinum on honeycomb-like NiO@Ni film as a synergistic electrocatalyst for the hydrogen evolution reaction. *ACS Catal* 2018;8(9):8866–72.
- [19] Zhang C, Qian L, Zhang K, Yuan S, Xiao J, Wang S. Hierarchical porous NiNiO core-shells with superior conductivity for electrochemical pseudo-capacitors and glucose sensors. *J Mater Chem A Mater Energy Sustain* 2015;3(19):10519–25.
- [20] Cheng G, Yang W, Dong C, Kou T, Bai Q, Wang H, et al. Ultrathin mesoporous NiO nanosheet-anchored 3D nickel foam as an advanced electrode for supercapacitors. *J Mater Chem A Mater Energy Sustain* 2015;3(33):17469–78.
- [21] Wang X, Qiao L, Sun X, Li X, Hu D, Zhang Q, et al. Mesoporous NiO nanosheet networks as high performance anodes for Li ion batteries. *J Mater Chem A Mater Energy Sustain* 2013;1(13):4173.
- [22] Tian H, Zhu S, Xu F, Mao W, Wei H, Mai Y, et al. Growth of 2D mesoporous polyaniline with controlled pore structures on ultrathin MoS₂ nanosheets by block copolymer self-assembly in solution. *ACS Appl Mater Interfaces* 2017;9(50):43975–82.
- [23] Liu L, Li Y, Yuan S, Ge M, Ren M, Sun C, et al. Nanosheet-based NiO microspheres: controlled solvothermal synthesis and lithium storage performances. *J Phys Chem C* 2010;114(1):251–5.
- [24] Xia K, Yang C, Chen Y, Tian L, Su Y, Wang J, et al. *In situ* fabrication of Ni(OH)₂ flakes on Ni foam through electrochemical corrosion as high sensitive and stable binder-free electrode for glucose sensing. *Sens Actuators B Chem* 2017;240:979–87.
- [25] Liu P, Ran J, Xia B, Xi S, Gao D, Wang J. Bifunctional oxygen electrocatalyst of mesoporous Ni/NiO nanosheets for flexible rechargeable Zn–Air batteries. *Nano-Micro Lett* 2020;12(1):68.
- [26] Xia K, Li Z, Zhou X. Ultrasensitive detection of a variety of analytical targets based on a functionalized low-resistance AuNPs/ β -Ni(OH)₂ nanosheets/Ni foam sensing platform. *Adv Funct Mater* 2019;29(39):1904922.
- [27] Bindhu MR, Umadevi M. Antibacterial activities of green synthesized gold nanoparticles. *Mater Lett* 2014;120:122–5.
- [28] Nguyen DH, El-Safty SA. Synthesis of mesoporous NiO nanosheets for the detection of toxic NO₂ gas. *Chemistry* 2011;17(46):12896–901.
- [29] Kim SI, Thiyagarajan P, Jang JH. Great improvement in pseudocapacitor properties of nickel hydroxide via simple gold deposition. *Nanoscale* 2014;6(20):11646–52.
- [30] Wang D, Li Y. Bimetallic nanocrystals: liquid-phase synthesis and catalytic applications. *Adv Mater* 2011;23(9):1044–60.
- [31] Wang L, Lou Z, Wang R, Fei T, Zhang T. Ring-like PdO-decorated NiO with lamellar structures and their application in gas sensor. *Sens Actuators B Chem* 2012;171–2:1180–5.
- [32] Li L, Xu J, Lei J, Zhang J, McLarnon F, Wei Z, et al. A one-step, cost-effective green method to *in situ* fabricate Ni(OH)₂ hexagonal platelets on Ni foam as binder-free supercapacitor electrode materials. *J Mater Chem A Mater Energy Sustain* 2015;3(5):1953–60.
- [33] Ma L, Hu Y, Chen R, Zhu G, Chen T, Lv H, et al. Self-assembled ultrathin NiCo₂S₄ nanoflakes grown on Ni foam as high-performance flexible electrodes for hydrogen evolution reaction in alkaline solution. *Nano Energy* 2016;24:139–47.
- [34] Pramanik G, Humpolickova J, Valenta J, Kundu P, Bals S, Bour P, et al. Gold nanoclusters with bright near-infrared photoluminescence. *Nanoscale* 2018;10(8):3792–8.
- [35] Gao W, Nyein HYY, Shahpar Z, Fahad HM, Chen K, Emaminejad S, et al. Wearable microsensor array for multiplexed heavy metal monitoring of body fluids. *ACS Sens* 2016;1(7):866–74.
- [36] Cheng B, Zhou L, Lu L, Liu J, Dong X, Xi F, et al. Simultaneous label-free and pretreatment-free detection of heavy metal ions in complex samples using electrodes decorated with vertically ordered silica nanochannels. *Sens Actuators B Chem* 2018;259:364–71.
- [37] Connelly D, Faulkner C, Clifton PA, Grupp DE. Fermi-level doping for low-barrier Schottky source/drain transistors. *Appl Phys Lett* 2006;88(1):012105.
- [38] Tan Y, Xue X, Peng Q, Zhao H, Wang T, Li Y. Controllable fabrication and electrical performance of single crystalline Cu₂O nanowires with high aspect ratios. *Nano Lett* 2007;7(12):3723–8.
- [39] Kim S, Kim S, Jung K, Kim J, Jang J. Ideal nanoporous gold based supercapacitors with theoretical capacitance and high energy/power density. *Nano Energy* 2016;24:17–24.

- [40] Michaelson HB. The work function of the elements and its periodicity. *J Appl Phys* 1977;48(11):4729–33.
- [41] Wu H, Wang L. A study of nickel monoxide (NiO), nickel dioxide (ONiO), and Ni(O₂) complex by anion photoelectron spectroscopy. *J Chem Phys* 1997;107(1):16–21.
- [42] Wang Z, Sim A, Urban JJ, Mi B. Removal and recovery of heavy metal ions by two-dimensional MoS₂ nanosheets: performance and mechanisms. *Environ Sci Technol* 2018;52(17):9741–8.
- [43] Fan C, Chen L, Jiang R, Ye J, Li H, Shi Y, et al. ZnFe₂O₄ nanoparticles for electrochemical determination of trace Hg(II), Pb(II), Cu(II), and glucose. *ACS Appl Nano Mater* 2021;4(4):4026–36.
- [44] Sang S, Li D, Zhang H, Sun Y, Jian A, Zhang Q, et al. Facile synthesis of AgNPs on reduced graphene oxide for highly sensitive simultaneous detection of heavy metal ions. *RSC Adv* 2017;7(35):21618–24.
- [45] Deshmukh MA, Celiesiute R, Ramanaviciene A, Shirsat MD, Ramanavicius A. EDTA_PANI/SWCNTs nanocomposite modified electrode for electrochemical determination of copper(II), lead(II) and mercury(II) ions. *Electrochim Acta* 2018;259:930–8.
- [46] Mohan S, Srivastava P, Maheshwari SN, Sundar S, Prakash R. Nano-structured nickel oxide based DNA biosensor for detection of visceral leishmaniasis (Kala-azar). *Analyst* 2011;136(13):2845–51.